International Journal of Nanomedicine

Dovepress
open access to scientific and medical research

Open Access Full Text Article

ORIGINAL RESEARCH

Combinatorial Polydopamine-Liposome Nanoformulation as an Effective Anti-Breast Cancer Therapy

Wangxing Lu[1,*], Wenjie Liu[1,*], Anna Hu[1], Jian Shen[1], Hanxi Yi[2], Zeneng Cheng[1]

[1]Xiangya School of Pharmaceutical Sciences, Central South University, Changsha, 410000, People's Republic of China; [2]School of Basic Medical Science, Central South University, Changsha, 410000, People's Republic of China

*These authors contributed equally to this work

Correspondence: Hanxi Yi; Wenjie Liu, Email hanxiyi2022@csu.edu.cn; wenjie.liu@csu.edu.cn

Introduction: Drug delivery systems (DDSs) based on liposomes are potential tools to minimize the side effects and substantially enhance the therapeutic efficacy of chemotherapy. However, it is challenging to achieve biosafe, accurate, and efficient cancer therapy of liposomes with single function or single mechanism. To solve this problem, we designed a multifunctional and multimechanism nanoplatform based on polydopamine (PDA)-coated liposomes for accurate and efficient combinatorial cancer therapy of chemotherapy and laser-induced PDT/PTT.

Methods: ICG and DOX were co-incorporated in polyethylene glycol modified liposomes, which were further coated with PDA by a facile two-step method to construct PDA-liposome nanoparticles (PDA@Lipo/DOX/ICG). The safety of nanocarriers was investigated on normal HEK-293 cells, and the cellular uptake, intracellular ROS production capacity, and combinatorial treatment effect of the nanoparticles were assessed on human breast cancer cells MDA-MB-231. In vivo biodistribution, thermal imaging, biosafety assessment, and combination therapy effects were estimated based on MDA-MB-231 subcutaneous tumor model.

Results: Compared with DOX·HCl and Lipo/DOX/ICG, PDA@Lipo/DOX/ICG showed higher toxicity on MDA-MB-231 cells. After endocytosis by target cells, PDA@Lipo/DOX/ICG produced a large amount of ROS for PDT by 808 nm laser irradiation, and the cell inhibition rate of combination therapy reached up to 80.4%. After the tail vein injection (DOX equivalent of 2.5 mg/kg) in mice bearing MDA-MB-231 tumors, PDA@Lipo/DOX/ICG significantly accumulated at the tumor site at 24 h post injection. After 808 nm laser irradiation (1.0 W/cm^2, 2 min) at this timepoint, PDA@Lipo/DOX/ICG efficiently suppressed the proliferation of MDA-MB-231 cell and even thoroughly ablated tumors. Negligible cardiotoxicity and no treatment-induced side effects were observed.

Conclusion: PDA@Lipo/DOX/ICG is a multifunctional nanoplatform based on PDA-coated liposomes for accurate and efficient combinatorial cancer therapy of chemotherapy and laser-induced PDT/PTT.

Keywords: reactive oxygen species, photodynamic therapy, photothermal therapy, polydopamine, liposome

Introduction

According to the global cancer statistics 2018, breast cancer has the highest global incidence (28.9%) and mortality rates (23.0%) in women.[1] Chemotherapy, as a mainstay in clinical breast cancer treatment, is limited by severe side-effects resulting from the nonspecific drug distribution in the human body.[2–4] What is worse, a single therapeutic modality alone has shown restricted therapeutic efficacy during clinical applications.[5] Phototherapy,[6] including photodynamic therapy (PDT)[7,8] and photothermal therapy (PTT),[9–11] has been widely accepted as a potent therapy modality for cancer treatment, due to the merits of excellent controllability, non-invasive property, minimal side effects, and so on.[12–14] PDT significantly increases the reactive oxygen species (ROS) levels in tumor cells by light-activated photosensitizers (PSs).[15–17] PDT relies on locally produced cytotoxic ROS to kill cancer cells, leaving normal tissue without light irradiation be free from damage.[17–20] PTT takes use of near infrared (NIR) light-absorbing agents to transfer light energy

Received: 14 July 2022
Accepted: 27 January 2023
Published: 17 February 2023

into hyperthermia, eventually resulting in thermal ablation of cancer cells, and the heat generated can be monitored by real-time photothermal imaging.[21–23] It is worth noting that the combination of PTT and PDT can achieve a more synergistic therapeutic effect.[24] On the one hand, thermal energy induced by PTT can promote cells to produce ROS to improve PDT efficacy.[25,26] On the other hand, tumor cells are more sensitive to the hyperthermia produced by PTT due to the promotion of ROS.[27] Therefore, phototherapy can be combined with chemotherapy to achieve greater tumor destruction or even thoroughly ablate tumor by different mechanisms.[28–30] Indocyanine green (ICG) as the FDA-approved PS and photothermal agent in clinical application,[31] which also acts as a NIR fluorescence imaging (FI) and photoacoustic imaging (PAI) dye, can induce hyperthermia for PTT and produce cytotoxic ROS for PDT simultaneously.[32] Nevertheless, the actual applications of ICG have been hindered seriously by its poor stability, quick elimination and weak targeting ability.[33]

In recent decades, multifunctional nanomaterial-based combination treatments have drawn much attention because of great efficacy and low side effects.[34] Various nanocarriers, including liposomes,[35,36] polymer materials,[37,38] inorganic nanoparticles, etc.,[39,40] have been explored to encapsulate ICG for avoiding these problems of free ICG molecules. Compared to other nanocarriers, it is proverbial that lipid-based nanoparticles with low toxicity and outstanding biocompatibility have been proven to be the most clinically established drug delivery systems.[41,42] Doxil®, doxorubicin (DOX) liposome, is one of the earliest clinical examples for cancer therapy.[43,44] However, liposomes have been greatly limited due to their premature drug leakage caused by inherent instability and the payload loss or undesired mixing caused by falling surface tension.[45] Fortunately, these problems can be overcome by the modification of the surface of liposomes with suitable polymers.[46,47] Polydopamine (PDA)-based organic nanoparticles have been reported to be superior to other polymers due to its reactive functional groups, simple modification technologies, non-cytotoxicity and excellent biocompatibility.[48–50] Due to its superior adhesion, PDA can be easily and strongly deposited on either organic or inorganic solid substrates with nucleophilic groups, such as, liposomes,[51,52] graphene oxide,[53,54] and cerium oxide[55] to improve haemocompatibility significantly of pristine carriers.[56] It is noteworthy that PDA-based nanoparticles (NPs) are pH-sensitive, which means that the release behaviors of loaded drug molecules can be accelerated at acidic conditions (pH < 6.0) of tumor tissues[57,58]. In addition, PDA has been demonstrated as exceptional PTT agents with strong photothermal conversion efficiency (>40%) under 808 nm laser irradiation.[59] NIR laser-controlled drug release from the PDA-based NPs can be achieved by decreased hydrogen bonding interaction between PDA and drugs due to the increasable heat of PTT effect.[60]

In this study, ICG and DOX were co-incorporated into the lipid bilayer, which were further coated with PDA by a facile two-step method to construct PDA-liposome NPs (PDA@Lipo/DOX/ICG) (Figure 1). PDA layer not only

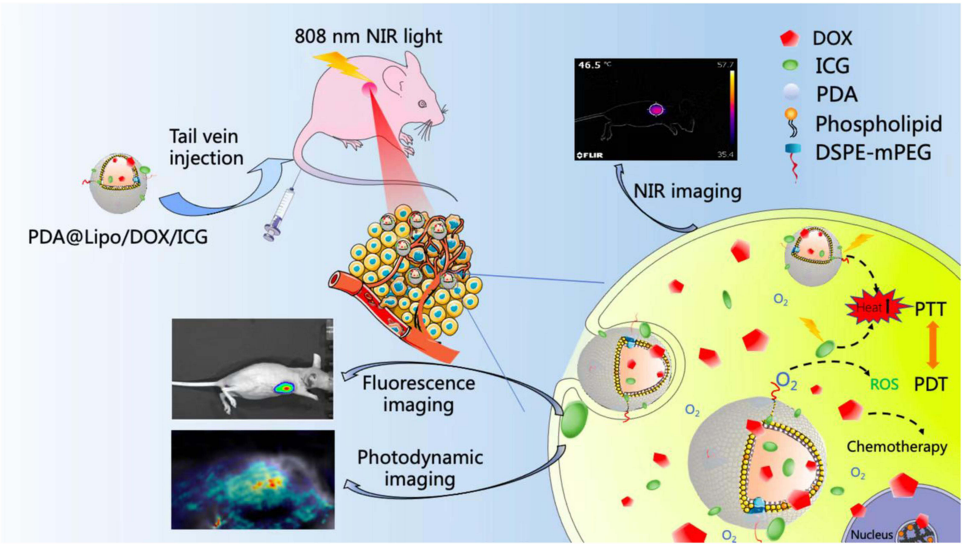

Figure 1 Schematic illustration of combination treatment and imaging of PDA@Lipo/DOX/ICG.

prevented undesired release of ICG and DOX encapsulated in liposomes to minimize the side effects but also enhances the photothermal effect with 808 nm laser irradiation. Via intravenous injection, PDA@Lipo/DOX/ICG was passively targeted in tumor sites, which could be monitored by the fluorescence (only ICG) and photoacoustic dual-modal imaging of ICG and PDA. ICG not only produced ROS to participate in PDT but also converted the NIR light energy into local hyperthermia for PTT, which was significantly enhanced by the synergistic effect of PDA. Acidic conditions of tumor sites and NIR laser irradiation significantly increased the release of DOX from the PDA-based NPs for subsequent chemotherapy. Above all, we constructed a multifunctional nanoplatform based on PDA-coated liposomes for accurate and efficient combinatorial tumor therapy of chemotherapy and laser-induced PDT/PTT.

Methods

The Synthesis of PDA@Lipo/DOX/ICG

To prepare PDA@Lipo/DOX/ICG, 32 mg HPSC, 10 mg cholesterol, 10 mg DSPE-mPEG2000, 4 mg DOX, and 2 mg ICG were co-dissolved in 2 mL methanol solvent. The organic phase was dropwisely added into 10 mL ultrapure water under 80 rpm stirring at 55 °C. After removing the methanol solvent by evaporation, the obtained solution was centrifuged (4000 rpm, 5 min) to remove unloaded DOX and ICG, further sonicated by an ultrasonic cell disruption system (120 W, 3 s, on, 3 s, off, 3 min), and then passed through 0.45 μm water-based filter to obtain homogeneous liposomes (Lipo/DOX/ICG).

0.5 mg/mL of DA·HCl was dissolved in 10 mL Tris-HCl (10 mM) at pH 8.5 and gradually polymerized under stirring at room temperature. After continuously stirring for 24 h, the synthesized PDA solution was then washed twice with ultrapure water by repeated centrifugation at 12,000 rpm for 10 min and stored at 4 °C in the dark for use. Afterwards, methanol solvent including 4 mg DOX and 2 mg ICG was added dropwise into 10 mL reacted PDA solution, further stirring for 12 h at 40 °C. PDA nanoparticles (NPs) loaded with drugs (PDA/DOX/ICG) were obtained following purification by dialysis.

Four-milliliter Lipo/DOX/ICG was immersed into 3 mL Tris-HCl buffer (10 mM) under a weakly alkaline environment (pH 8.5), which contained 1.5 mg of DA·HCl, to polymerize a PDA layer on the surface of Lipo/DOX/ICG. Subsequently, the suspension was continuously stirred (80 rpm) for 12 h at room temperature until the solution darkened, which demonstrated PDA@Lipo/DOX/ICG was obtained.

Drug-free Liposomes (Lipo), PDA, and PDA@liposome (PDA@Lipo) NPs were prepared by the same method above, but no drugs were added during the process. All samples were sealed at 4 °C for further study.

The Characterization of PDA@Lipo/DOX/ICG

The surface morphology of PDA@Lipo/DOX/ICG, PDA/DOX/ICG, and Lipo/DOX/ICG was characterized by transmission electron microscopy (TEM, JEOL JEM1200EX, Japan). Malvern Zetasizer Nano Series instrument (Zetasizer Nano-ZS, Malvern Instruments, UK) was utilized to measure their sizes, polydispersity indexes (PDIs) and Zeta potentials. The aforementioned formulations were monitored by UV-Vis-NIR spectrometer (UV-2600, Japan) and the Fourier transform infrared (FTIR) spectrometer (Bruker, Germany). After ultrafiltration centrifugation and methanol extraction, the encapsulation efficiency (EE) and drug loading capacity (LC) of DOX in the NPs were quantified and calculated using high-performance liquid chromatography (HPLC) analysis (Agilent, Santa Clara, USA). In detail, 200 μL NPs in ultrafiltration centrifuge tube was centrifuged at 4000g for 15 min. The upper filter residue was concentrated NPs, and the free drugs were located in the filtrate. The total DOX in the NPs was determined by disrupting the mixture with methanol. The mobile phase was 0.01 mol/L potassium dihydrogen phosphate solution/acetonitrile (72:28, v/v), and the total flow rate was 1.0 mL/min. The detection wavelength was set at 254 nm. EE and LC were calculated as follows:

$$\mathrm{EE} = (\text{total amount of DOX} - \text{amount of free DOX})/\text{total amount of DOX} \times 100\%$$

$$\mathrm{LC} = (\text{total amount of DOX} - \text{amount of free DOX})/\text{amount of NPs} \times 100\%$$

Dialysis method was adopted to compare DOX release behaviours from PDA@Lipo/DOX/ICG, PDA/DOX/ICG, or Lipo/DOX/ICG. In brief, solutions of different NPs (1.0 mL) in dialysis bags (MwCO = 3500) were placed into 30 mL

PBS (pH 7.4) and oscillated (100 rpm, 37 °C). At certain time points (0.5, 1, 2, 4, 6, 8, and 12 h), 200 μL PBS solution was collected for DOX quantification by HPLC, and replaced with fresh PBS solution. The DOX release behaviours of PDA@Lipo/DOX/ICG were investigated in different pH release media (pH = 7.4, 5.0) with or without laser irradiation at 0.5 h (2.0 W/cm^2, 5 min). Each experiment was determined in triplicate.

The Stability of PDA@Lipo/DOX/ICG

To test the stability of NPs in different physiological solutions, 2 mL PDA@Lipo/DOX/ICG, PDA/DOX/ICG, or Lipo/DOX/ICG were put into ultrapure water or FBS (NPs: media = 1:1, v/v), respectively, and incubated at 4 °C. Samples were taken and analyzed for size distribution and content at certain time periods (1, 2, 5, 10, and 15 d).

The in vitro Singlet Oxygen ($^1O_2$) Detection and Photothermal Effect of PDA@Lipo/DOX/ICG

DPBF, with a characteristic absorption peak at 417 nm, was used to evaluate the in vitro $^1O_2$ generation capability of PDA@Lipo/DOX/ICG.[61,62] Briefly, 3 mL of PBS, free ICG and PDA@Lipo/DOX/ICG containing 5 μM DPBF were irradiated by 808 nm laser (VA-I-DC, Beijing Viasho Technology Co., Ltd.) with the power intensity of 1.0 W/cm^2, and the absorbance of DPBF was measured every 1 min by a UV-vis-NIR spectrometer.

To compare the photothermal performance of different formulations, 1 mL H2O, blank carrier PDA, Lipo/DOX/ICG, and PDA@Lipo/DOX/ICG were irradiated by 808 nm laser (2.0 W/cm^2). The temperature was monitored every 1 min for ten cycles by an infrared thermal imaging camera (FLIR E50, Estonia). Photothermal effect of PDA@Lipo/DOX/ICG was further analyzed with different power densities (0.5, 1.0 and 2.0 W/cm^2), and the laser irradiation time varied from 1 to 10 min.

Cell Culture

The human breast cancer cells MDA-MB-231 and normal human embryonic kidney cells HEK293 were obtained from XiangYa Central Experiment Laboratory (Hunan, China), which were cultured in Dulbecco's Modified Eagle's Medium (DMEM) supplemented with 10% (v/v) fetal bovine serum (FBS) and 1% (v/v) penicillin-streptomycin, in a humidity atmosphere containing 5% CO_2 at 37 °C.

The Cellular Uptake of PDA@Lipo/DOX/ICG

The cellular uptake of PDA@Lipo/DOX/ICG was qualitatively visualized by inverted fluorescence microscopy (Olympus, Germany). MDA-MB-231 cells were incubated overnight in 12-well plates (1×10^5 cells per well). Then, PDA@Lipo/DOX/ICG was added with DOX concentration of 10 μg/mL and further incubated for different time periods (0, 2, 6, and 12 h). Subsequently, the cells were rinsed twice with PBS, fixed with 4% paraformaldehyde for 10 min. Finally, cells were stained with Hoechst 33342 (10 μM) for 10 min and thoroughly washed prior to FI.

To analyze the fluorescence intensity quantitatively, flow cytometry (FACS Verse, USA) was carried out, and the previous operation was performed in the same manner as above. After incubating for different time periods (1, 2, 6, 12, and 24 h), the cells were collected and analyzed using a flow cytometer.

The Intracellular ROS Detection of PDA@Lipo/DOX/ICG

Intracellular ROS detection of PDA@Lipo/DOX/ICG was measured using DCFH-DA fluorescent probe, which can be rapidly oxidized into DCF with green fluorescent in the presence of ROS.[23] Briefly, MDA-MB-231 cells were seeded in 6-well plates (5×10^5 cells per well) and incubated overnight. ROS inhibitor NaN_3 was added and incubated for another 12 h, depleting the ROS produced by MDA-MB-231 cells themselves. Then, two different concentrations of PDA@Lipo/DOX/ICG (10 μg/mL, 20 μg/mL) were added for 2 h incubation. After washing thrice with PBS, the cells were cultured with 2 mL of DCFH-DA (10 μM) for 30 min. Finally, after being irradiated for 2 min (1.0 W/cm^2), the cells were trypsinized and resuspended in 1.0 mL PBS, followed by flow cytometry analysis with 488 nm excitation.

The in vitro Cytotoxicity of PDA@Lipo/DOX/ICG

The in vitro cytotoxicity studies were assessed on HEK293 and MDA-MB-231 cells by MTT method. To verify the safety of blank carriers, HEK293 cells (1×10^4 cells per well) were cultured in 96-well plates for 24 h. Then, the cells were treated with PDA, PDA + NIR, Lipo, Lipo + NIR, PDA@Lipo, and PDA@Lipo + NIR at different concentrations in media, and 808 nm laser irradiation (1.0 W/cm^2, 2 min) was given after 8 h incubation in laser-irradiated groups. Twenty-four hours later, cells were treated with 20 μL MTT solution (5 mg/mL) and incubated continued for 4 h. Finally, cell viability was evaluated using ELISA plate reader (TECAN, Austria) after reacting with 150 μL DMSO under mild shaking at 37 °C.

For the cytotoxicity assay of NPs, MDA-MB-231 cells were divided into five groups, including free DOX·HCl, Lipo/DOX/ICG, Lipo/DOX/ICG + NIR, PDA@Lipo/DOX/ICG, and PDA@Lipo/DOX/ICG + NIR, and tested using the above-mentioned procedure. The cell inhibition rates of five groups were compared at a range of concentrations.

To visualize the combination therapy cytotoxicity of PDA@Lipo/DOX/ICG, we used Calcein-AM and 0.4% trypan blue staining live and dead cells separately to imaging as the qualitative method. Specifically, MDA-MB-231 cells were seeded in 24-well culture plate (1×10^5 cells per wall) for 24 h incubation and treated with different concentrations of PDA@Lipo/DOX/ICG (5 μg/mL, 10 μg/mL, 30 μg/mL) for another 8 h incubation. Afterwards, the cells were irradiated for 2 min (1.0 W/cm^2) and continued to incubate for 12 h. Finally, the cells were stained with Calcein-AM and 0.4% trypan blue, and rinsed with PBS thoroughly to observe with Inverted fluorescence microscope.

Tumor Models

BALB/c nude mice (female, 4–5 weeks) were conducted under a protocol approved by the Animal Ethics Committee of Central South University in compliance with the National Institutes of Health guide for the care and use of Laboratory animals (NIH Publications No. 8023, revised 1978) and were acclimated to standard diet at 25 °C for 1 week prior to the study. MDA-MB-231 cells (2×10^6) were injected subcutaneously in the right forelimb of the mice to establish breast cancer tumor-bearing models. Tumor volume was calculated as follows: tumor volume = length × (width)^2/2.

The in vivo FI and PAI of PDA@Lipo/DOX/ICG

First, tumor-bearing mice with a volume of about 200 mm^3 were randomly selected. Experimental group mice were injected with 200 μL of PDA@Lipo/DOX/ICG nanoparticle solution via tail vein, and the control group mice were injected with an equal amount of free ICG as a control. After 1 h and 24 h administration, respectively, the mice were anesthetized with isoflurane and then placed in IVIS Spectrum imaging system (Perkin Elmer, USA) for comparison and observation (Ex: 745 nm, Em: 820 nm). Finally, the mice were sacrificed, and their tumor tissues and main organs (heart, liver, spleen, lung, and kidney) were obtained for the ex vivo imaging. For the PAI, photoacoustic signals of tumor-bearing mice were monitored using a VEVO LASER PAI system (VEVO 2100, FUJIFILM Visual Sonics, INC, USA) at different time points.

The in vivo Antitumor Efficiency of PDA@Lipo/DOX/ICG

When the tumor volumes reached about 100 mm^3, the tumor-bearing mice were randomly divided into seven groups (n = 5): (1) PBS; (2) PBS + NIR; (3) free DOX·HCl; (4) Lipo/DOX/ICG; (5) Lipo/DOX/ICG + NIR; (6) PDA@Lipo/DOX/ICG; (7) PDA@Lipo/DOX/ICG + NIR (DOX equivalent of 2.5 mg/kg). Then, the treatment was carried out by intravenous injection, and the three laser groups were irradiated for 24 h after injection at a power intensity of 1 W/cm^2 for 2 min. The temperature changes in tumors during irradiation were monitored using an infrared thermal imaging camera.

DOX·HCl group was injected every 3 days for a total of 5 administrations, and other groups were injected only once during the treatment cycle. The tumor sizes and body weights of mice in the groups were recorded every 3 days. Twenty-one days later, all the mice were sacrificed, and their tumors and major organs were resected, weighed (only tumors), and fixed in formalin for paraffin embedding to hematoxylin and eosin (H&E) analysis and Tunel staining (only tumors).

Inhibition rates of tumor growth (IRT) were calculated as follows: IRT = (mean tumor weight of the PBS group – mean tumor weight of the experimental group)/mean tumor weight of the PBS group × 100%.

Statistical Analysis

The statistical analysis (*t*-test) was carried out by OriginPro 9.0 (OriginLab, MA, USA). All statistical analyses were shown as mean ± standard deviation (SD), *p < 0.05 or less was considered statistically significant (NS, no significance, *p < 0.05, **p < 0.01, ***p < 0.001, ****p < 0.0001).

Results and Discussion

The Synthesis and Characterizations of PDA@Lipo/DOX/ICG

Lipo/DOX/ICG NPs were firstly prepared through a methanol injection method, and wherefore DOX/ICG was encapsulated in liposomes. A PDA-coating was developed on the surface of Lipo/DOX/ICG NPs to form PDA@Lipo/DOX/ICG NPs in an alkaline condition (pH = 8.5). The whole synthesis method was universal and straightforward, and all it needed was a brief stirring under alkaline conditions to obtain PDA coated liposomes. To compare the difference between drug delivery systems, PDA/DOX/ICG NPs were also prepared by an oxidative polymerization reaction.[52]

FTIR spectra were used to investigate the disappearance, movement or broadening of the characteristic peaks of PDA coated liposomes, which can indicate the interaction between different materials.[63] As shown in Figure 2A, PDA, Lipo, and PDA@Lipo all exhibit obvious characteristic peaks from 3615 cm^{-1} to 3100 cm^{-1}, which might be caused by the stretching vibration of the water hydroxyl O-H in the water-soluble system.[64] In the meantime, the two characteristic peaks located at 2960 cm^{-1} and 2870 cm^{-1} are corresponded to the stretching vibration of C-H, which prove that the structures of three blank carriers all contain methyl groups. In addition, the characteristic peaks of C=O (1750 cm^{-1}) and phosphate ester (1250 cm^{-1}) are attributed to blank Lipo, while the characteristic peak at

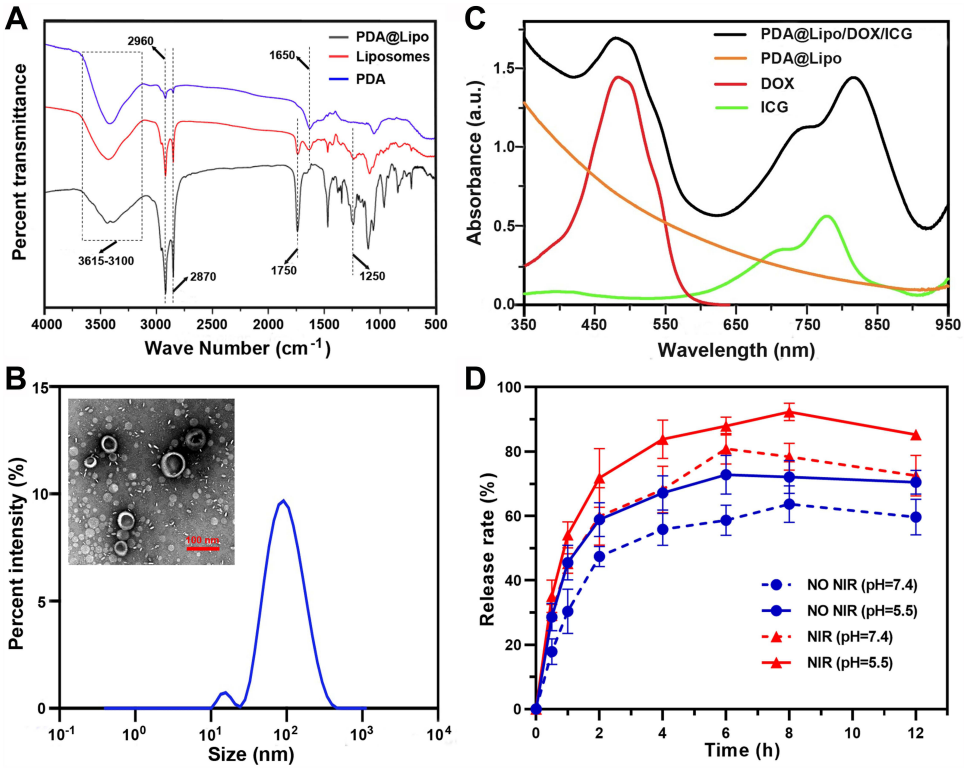

Figure 2 (**A**) FTIR spectra of blank carriers PDA, Liposomes, and PDA@Lipo. (**B**) Sizes and morphology of PDA@Lipo/DOX@ICG measured using a Malvern Zetasizer Nano Series instrument and TEM. Scale bar for TEM is 100 nm. (**C**) UV-vis-NIR spectra of DOX, ICG, PDA@Lipo, and PDA@Lipo/DOX@ICG. (**D**) DOX release from PDA@Lipo/DOX@ICG in different pH release media (pH = 7.4, 5.0) with or without laser irradiation (2.0 W, 5 min) at 0.5 h (n = 3 per group).

1650 cm^{-1} is assigned to the C=C skeleton stretching vibration of benzene rings in PDA. Further comparison shows that PDA@Lipo has both the characteristic absorption peaks of PDA (C=C on the benzene ring) and Lipo (carbonyl and phosphate), indicating the successful conjugation of PDA@Lipo.

The morphologies of NPs were measured by TEM and shown in Figure 2B and Supplementary Figure S1a and b, which all present almost spherical shapes. However, Lipo/DOX/ICG NPs vary in size and had adhesion, indicating that there might be a fusion phenomenon (Supplementary Figure S1a); PDA/DOX/ICG also displays partial aggregation (Supplementary Figure S1b). In contrast, PDA@Lipo/DOX/ICG NPs (Figure 2B) are more dispersed, and there is a clear visible core-shell structure, which indicates the successful deposition of PDA film coating on the liposomes.

The sizes and PDIs of NPs are shown in Figure 2B, Supplementary Figure S1a and b, and Table 1. PDA/DOX/ICG NPs have a mean particle size of 285.4 nm, Lipo/DOX/ICG NPs are measured as 99.8 nm, while that of PDA@Lipo/DOX/ICG NPs are 167.1 nm. Thus, the thickness of the coated PDA film is approximately 30 nm. Compared to the size obtained from TEM, the sizes measured by Malvern Zetasizer Nano Series instrument are relatively larger, which might be caused by the potential slight clustering and hydration effect.[5] This phenomenon also proves that the PDA film was successfully formed on the surface of Lipo/DOX/ICG. The small size of PDA@Lipo/DOX/ICG means that it is easy to permeate into tumor tissue through the EPR effect.[65] The particle size peak is unimodal, symmetrical and concentrated, indicating that this system is relatively stable, and the PDI <0.2 indicates a homogenous dispersion. In contrast, the PDI value of Lipo/DOX/ICG and PDA/DOX/ICG is more than 0.2, and the particle size peak of Lipo/DOX/ICG is bimodal, indicating that the particle distribution is poor and might be agglomerated Zeta potential is an important indicator of the stability of the dispersion system. A higher absolute value indicates larger mutual repulsion between the NPs, and a more stable dispersion system. The results of Zeta potential are displayed in Table 1. The Zeta potential of the blank liposomes is positive and small, while the Zeta potential of PDA@Lipo is changed to negative after coating by PDA since PDA is a negative polyelectrolyte which could increase the negative charge of the entire system.[66] Similarly, the absolute value of PDA@Lipo/DOX/ICG was much higher than that of Lipo/DOX/ICG, which increased the mutual repulsion between the NPs, making the entire system more stable. The characteristic peaks of UV absorption for free DOX and ICG appear at 490 nm and 750–800 nm, respectively.[67,68] To verify whether DOX and ICG were successfully encapsulated into PDA@Lipo/DOX/ICG, we characterized the formulation by UV-vis-NIR spectroscopy, and the characteristic peaks of free DOX and ICG were observed in PDA@Lipo/DOX/ICG (Figure 2C). The blank carrier PDA@Lipo has broad-spectrum absorption characteristics in the range of 350–850 nm, and its intensity is proportional to the concentration (Supplementary Figure S1c). Notably, there is a slight red-shift from 780 nm to 815 nm in the absorption spectra of PDA@Lipo/DOX/ICG compared to that of free ICG, which can be ascribed to the close-packed ICG in the NPs or the aggregation of ICG induced by the addition of DOX, and the aggregated ICG absorbs at a longer wavelength compared to a single ICG molecule.[68–70]

The LC, EE and content of DOX are also illustrated in Table 1. Since PDA is water-soluble and difficult to load fat-soluble drugs, the EE of PDA/DOX/ICG is only 23.5%. Both the EE (85.4%) and LC (3.4%) of Lipo/DOX/ICG are low, which might be related to the drug leakage of liposomes. After the PDA coating, the EE of PDA@Lipo/DOX/ICG is close to 100%, and the LC (5.7%) is higher than that of Lipo/DOX/ICG, which indicates the PDA coating could reduce the leakage of free DOX. However, the added volume of PDA also diluted the concentration of DOX resulting in the content of PDA@Lipo/DOX/ICG lower than that of Lipo/DOX/ICG.

Table 1 Characterization (Sizes, PDIs, Zeta Potentials, Drug Loading and Contents of DOX) of Different NPs

NPs	Size (nm)	PDI	Zeta (mV)	EE (%)	LC (%)	C (μg/mL)
PDA	132.4	0.13	−40.9	–	–	–
Lipo	83.5	0.23	1.0	–	–	–
PDA@Lipo	144.2	0.18	−10.3	–	–	–
PDA/DOX@ICG	285.4	0.25	−5.1	23.8	9.4	47.6
Lipo/DOX@ICG	99.8	0.29	−7.3	85.4	3.4	345.8
PDA@Lipo/DOX@ICG	167.1	0.18	−25.4	98.9	5.7	154.9

To explore the drug release process, the formulations were sealed in dialysis bags under different pH release media (pH = 7.4, 5.0) with or without irradiation, and the release profiles of DOX were recorded by monitoring the drug concentration outside the bag using HPLC. As observed in Supplementary Figure S1d, PDA/DOX/ICG and Lipo/DOX/ICG show a rapid release (>30%) within 0.5 h, while the release rate of PDA@Lipo/DOX/ICG (Figure 2D) is delayed. This property might attribute to the package of PDA film, which is dissolved and degraded slowly. Compared with in PBS (pH = 7.4), the cumulative release of the three NPs both has a certain increase at pH 5.5, which could be attributed to the protonated amino group of DOX to provide a positive charge to improve the solubility in acidic solutions, thereby induces the release of DOX.[50] Moreover, whether at pH 7.4 or pH 5.5, irradiation added could improve the total amount of released DOX from PDA@Lipo/DOX/ICG significantly, from 63.67% to 72.13% and from 78.32% to 92.31% at pH 7.4 and pH 5.5, respectively. The promotion of DOX release is attributed to the photothermal effects of PDA and ICG in PDA@Lipo/DOX/ICG. On the one hand, the heat could destroy the PDA film to promote the release of DOX; on the other hand, the high temperature accelerates the diffusion of DOX molecules.

The Stability of PDA@Lipo/DOX/ICG

In order to compare the stability of the different prepared NPs, the sizes were monitored. As shown in Supplementary Figure S2a, PDA/DOX/ICG had a significant increase in particle sizes in the two physiological solutions. Especially, the size of NPs in FBS exceeded 1500 nm after only one day, and exceeded 3000 nm after 15 days. Combined with Supplementary Figure S2b, black precipitates of PDA/DOX/ICG in water and FBS solutions could be seen clearly, which show that PDA/DOX/ICG is very unstable with poor dispersibility. Therefore, PDA/DOX/ICG has not been studied in subsequent cell and animal experiments. Lipo/DOX/ICG also occurred aggregation 15 days later. In contrast, size of PDA@Lipo/DOX/ICG had no obvious change 15 days later (Figure 3A), and no obvious aggregation phenomenon of PDA@Lipo/DOX/ICG could be observed in both aqueous solution and FBS (Figure 3B), indicating that the stability of PDA@Lipo/DOX/ICG is superior to PDA/DOX/ICG and Lipo/DOX/ICG.

The drug contents of the NPs in water and FBS over time were further compared. The results show that the contents of the three kinds of NPs decreased gradually with time, and the contents of NPs in FBS decreased relatively faster (Figure 3C and Supplementary Figure S2c). After 15 days, DOX contents in both PDA/DOX/ICG and Lipo/DOX/ICG decreased by more than 50% (Supplementary Figure S2c), while DOX levels in PDA@Lipo/DOX/ICG remained stable (Figure 3C).

The in vitro $^1O_2$ Detection and Photothermal Effect of PDA@Lipo/DOX/ICG

To detect the PDT property, DPBF was used as a capture agent for $^1O_2$, which can quickly react with $^1O_2$ to reduce its absorption intensity at 417 nm, and the greater the decrease in absorbance, the higher the $^1O_2$ generation.[71] The absorption intensity at 417 nm of free DPBF hardly changed within 10 minutes, indicating that there was basically no generation of $^1O_2$ (Supplementary Figure S3a), but the free ICG (Supplementary Figure S3b) and PDA@Lipo/DOX/ICG

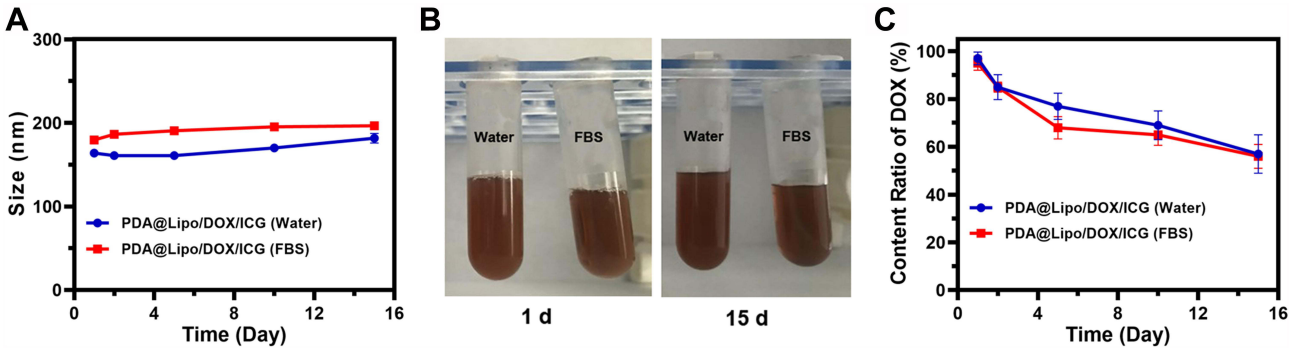

Figure 3 (**A**) The change of particle sizes of PDA@Lipo/DOX@ICG in aqueous solution and FBS. (**B**) The appearance comparison of PDA@Lipo/DOX@ICG before and after storage. (**C**) The content change of PDA@Lipo/DOX@ICG in water and FBS.

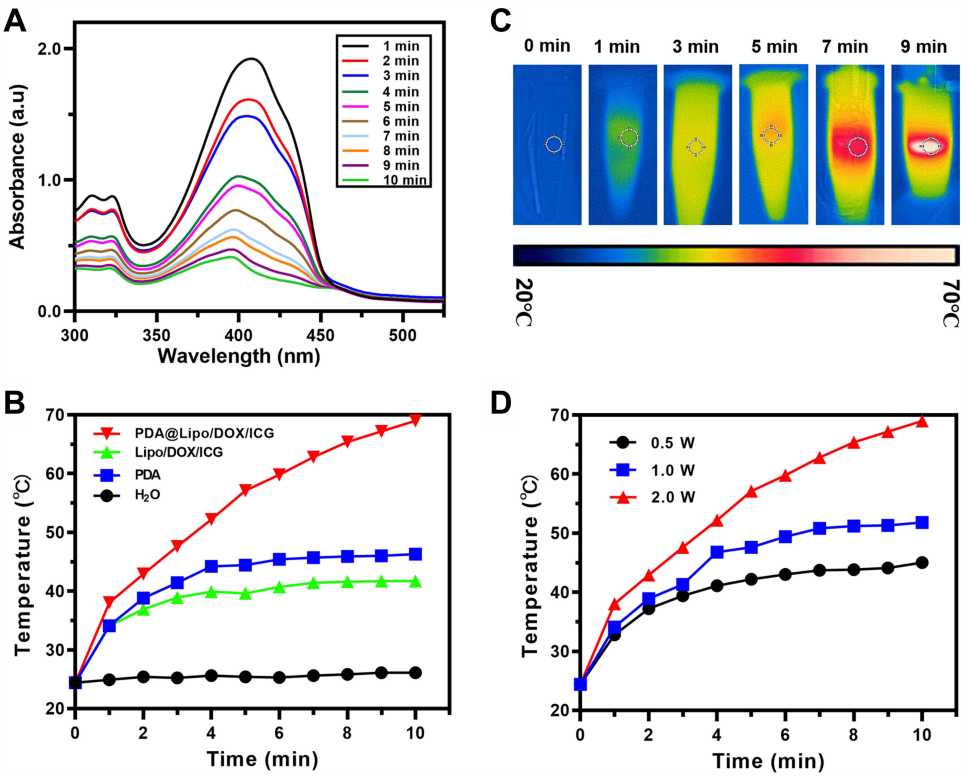

Figure 4 (**A**) In vitro $^1O_2$ detection of PDA@Lipo/DOX@ICG using $^1O_2$ probe DPBF, whose attenuation rate at 417 nm is directly proportional to the generation rate of $^1O_2$ under 808 nm laser radiation (1.0 W/cm^2, 10 min). (**B**) Temperature rise profiles of PDA/DOX@ICG, Lipo/DOX@ICG groups, H_2O and PDA group (The amount of blank carrier PDA is equivalent to that of PDA@Lipo/DOX@ICG) under 808 nm laser irradiation (2.0 W/cm^2, 10 min). (**C**) Infrared thermographic maps of PDA@Lipo/DOX@ICG at different time points under 808 nm laser irradiation (2.0 W/cm^2). (**D**) Temperature rise profile of PDA@Lipo/DOX@ICG under different power irradiation (0.5, 1.0, 2.0 W/cm^2).

NPs (Figure 4A) resulted in a decreased absorption intensity of DPBF at 417 nm gradually with the increase of irradiation time, implying the strong $^1O_2$ generation ability and great PDT property of PDA@Lipo/DOX/ICG NPs.

The photothermal performances of H_2O, blank carrier PDA, Lipo/DOX/ICG, and PDA@Lipo/DOX/ICG were measured by infrared imager under the irradiation of an 808 nm laser (2.0 W/cm^2, 10 min). As shown in Figure 4B, the temperature of water varies from 23.4 °C to 26.7°C, while the temperature increases of PDA, Lipo/DOX/ICG, and PDA@Lipo/DOX/ICG are 21.9 °C, 17.3 °C, and 48.6 °C, respectively. Interestingly, PDA@Lipo/DOX/ICG showed better photothermal effect than PDA/DOX/ICG, the reason might be that the ICG loading capacity of water-soluble PDA was weak, and lower concentration of ICG resulted in limited photothermal property. PDA@Lipo/DOX/ICG exceeds 50 °C in less than 4 minutes and reaches 69.0 °C after 10 minutes irradiation, which performs obvious time-dependent photothermal characteristics. Because the photothermal effect of PDA@Lipo/DOX/ICG comes from PDA and ICG, it is stronger than that of single carrier PDA or Lipo/DOX/ICG.

In addition, the relationship between thermal performance and irradiation power for PDA@Lipo/DOX/ICG was examined. As shown in Figure 4C and D, by improving the power density of irradiation, the temperature is significantly increased. Especially at 2.0 W/cm^2, the temperature increases closed to 70 °C, indicating the exceptional PTT effect of the optimal formulation. Considering that too high temperature may exceed the skin tolerance and cause damage to normal cells, 1.0 W/cm^2 was used in the subsequent cell and animal experiments.

The Cellular Uptake of PDA@Lipo/DOX/ICG

The cellular uptake of PDA@Lipo/DOX/ICG was observed by inverted fluorescence microscopy (Figure 5A). After incubation for 2 h, red fluorescence of DOX was found in the cells. The fluorescence intensity was enhanced by prolonging the incubation time. The cells showed obvious red fluorescence at 12 h, indicating that PDA@Lipo/DOX/ICG NPs could successfully deliver DOX into cells. The quantitative determination of uptake ability of PDA@Lipo/DOX/

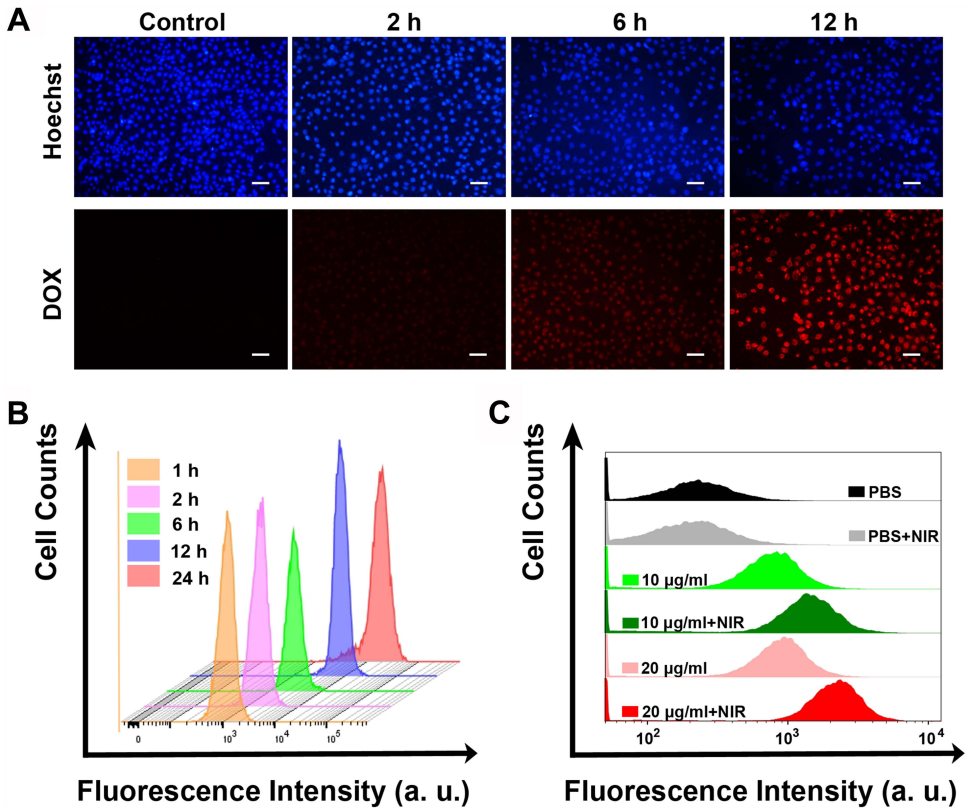

Figure 5 (**A**) Fluorescence images of MDA-MB-231 cells incubated with PDA@Lipo/DOX@ICG for 2, 6 or 12 h (The scale bar is 50 μm). (**B**) Flow cytometry analysis of MDA-MB-231 cells incubated with PDA@Lipo/DOX@ICG for different incubation periods (Ex: 505 nm, Em: 550 nm). (**C**) Flow cytometry analysis of intracellular ROS generation of PDA@Lipo/DOX@ICG with 1.0 W/cm^2 laser for different ICG concentrations (0, 10, and 20 μg/mL) inside MDA-MB-231 cells (ROS-sensitive probe DCFH-DA, Ex: 488 nm, Em: 525 nm).

ICG NPs in cells was also studied using flow cytometer. As seen in Figure 5B, the fluorescence intensity of DOX is directly proportional to the incubation time in a certain time period. After 12 h, the fluorescence intensity does not increase obviously, indicating that the cellular uptake has reached saturation.

The Intracellular ROS Detection of PDA@Lipo/DOX/ICG

Pretreated with NaN_3 to scavenge endogenous $^1O_2$ of MDA-MB-231 cells, the intracellular ROS produced by PDA@Lipo/DOX/ICG with irradiation was detected using an ROS-sensitive probe DCFH-DA. As shown in Figure 5C, the fluorescence intensity of PBS groups is basically unchanged with or without irradiation. As for the PDA@Lipo/DOX/ICG groups, the fluorescence intensity of irradiation groups is significantly higher than that of no irradiation groups, meaning that PDA@Lipo/DOX/ICG has produced an additional high level of ROS inside tumor cells by irradiation, which plays an indispensable role in PDT. Moreover, with the increase of drug concentration, the fluorescence intensity becomes stronger after irradiation, suggesting that ROS production is directly proportional to the cellular concentration of PDA@Lipo/DOX/ICG.

The in vitro Cytotoxicity Assay of PDA@Lipo/DOX/ICG

At first, the cytotoxicity of three carrier materials (PDA, Lipo, and PDA@Lipo) towards HEK293 cells was assessed using MTT assay. When the concentration of PDA was in the range of 10–200 μg/mL, the cell survival rates of the group without irradiation was more than 90%, indicating that PDA had biocompatibility and was basically non-toxic to HEK293 cells (Supplementary Figure S4a). As for Lipo and PDA@Lipo (Supplementary Figure S4b and Figure 6A), the cell survival rate also exceeded 80% as the concentration increased from 50 μg/mL to 1000 μg/mL, showing good biological safety. Moreover, after 1.0 W/cm^2 irradiation for 2 min, PDA and PDA@Lipo showed significant cytotoxicity

to cells with the increase of PDA concentration, while Lipo remained basically unchanged after irradiation. The results show the biosafety of PDA and Lipo and the photothermal effect of PDA.

Similarly, the inhibitory rate of different NPs towards MDA-MB-231 cells was also measured by MTT assay. As shown in Figure 6B, the cell inhibitory rates of all NPs gradually increase as the concentration increases, implying a concentration-dependent cytotoxic effect. Basically, both Lipo/DOX/ICG and PDA@Lipo/DOX/ICG NPs show a stronger cytotoxicity than free DOX·HCl at each corresponding concentration, suggesting that NPs can be better taken up by MDA-MB-231 cells than free DOX·HCl. For Lipo/DOX/ICG and PDA@Lipo/DOX/ICG, when the DOX concentrations are higher than 5 μg/mL, the inhibition rates of the irradiation groups are significantly higher than those of the no irradiation groups. In particular, the cell inhibition rate of PDA@Lipo/DOX/ICG + NIR group could reach 68.2% at a concentration of 10 μg/mL, while the cell inhibition rate of no irradiation group is less than 40%, indicating that combination of chemotherapy and phototherapy could achieve better antitumor effect at relatively low doses.

The induced apoptosis ability of different concentrations of PDA@Lipo/DOX/ICG was further visualized by staining dead cells with trypan blue and live cells with Calcein-AM. As shown in Figure 6C, both PBS group and PBS + NIR group exhibit intense green fluorescence and few staining blue, indicating almost all cells were intact and normal. In contrast, green fluorescent numbers are obviously reduced by increasing the DOX concentration in PDA@Lipo/DOX/ICG groups. This phenomenon is more obvious in PDA@Lipo/DOX/ICG + NIR groups, and only a few cells survived when the concentration of DOX was 10 μg/mL. When the concentration reached 30 μg/mL, almost all cells with no clear outline and complete morphology are stained by trypan blue. In vitro experiments, including cellular uptake, intracellular ROS detection, and cytotoxicity, confirm that PDA@Lipo/DOX/ICG could not only convert NIR light energy into local hyperthermia for PTT but also produce an additional high level of ROS to participate in PDT, indicating that the NPs have certain phototherapeutic effect. Moreover, the synergistic therapy efficacy of phototherapy and chemotherapy is far superior to that of chemotherapy alone.

The in vivo FI and PAI of PDA@Lipo/DOX/ICG

Both ICG and PDA have been widely explored as fluorescence (only ICG) and/or photoacoustic contrast agents because of their strong optical absorbance in the NIR region. Both FI and PAI are nonradioactive imaging methods with intrinsic advantages. FI could visualize the dynamic distribution of NPs throughout the whole body.[72,73] At the same time, PAI could monitor the accumulation of NPs within the deep regions of tumor with improved imaging resolution.[74] By injecting intravenously free ICG and PDA@Lipo/DOX/ICG, the in vivo FI of tumor and the major organs (heart, liver, spleen, lung, and kidney) were performed. Two hours later, the mice in both PDA@Lipo/DOX/ICG and ICG groups had obvious fluorescence signal all over the body (Figure 7A). After 24 h, fluorescence signals were obviously accumulated at the tumor sites in PDA@Lipo/DOX/ICG group. Due to its unique EPR effect, the fluorescence intensity was significantly stronger than that of other organs. On the contrary, free ICG was mainly distributed in the liver, and no obvious fluorescence signal was observed in the tumor.

To confirm tumor accumulation of the NPs through EPR effect, the tumor bearing mice were sacrificed 24 h post injection, and the tumors and major organs were collected for FI. Ex vivo imaging shows bright fluorescence at the tumor regions of mice treated with PDA@Lipo/DOX/ICG (Figure 7B). However, the free ICG is mainly distributed in the liver, and almost no fluorescence signal occurred in the tumor regions. As shown in Figure 7C, the fluorescence intensity of the tumor regions in PDA@Lipo/DOX/ICG group is approximately 10.6-fold higher than that in free ICG group, and also much higher than that of other organs within the group.

Subsequently, the in vivo PAI of PDA@Lipo/DOX/ICG was evaluated using a Vevo LAZR system.[75,76] After intravenous injection, the photoacoustic images of the mice in these groups were obtained at different time periods (Figure 7D and E). Owing to the rapid in vivo clearance of free ICG, no obvious signal was observed in tumor sites of free ICG group at any time points (Figure 7D and E). On the contrary, the signal intensity of PDA@Lipo/DOX/ICG in tumor sites gradually increased over time and reached the peak value at 24 h post injection, indicating deep accumulation of PDA@Lipo/DOX/ICG within the tumor.

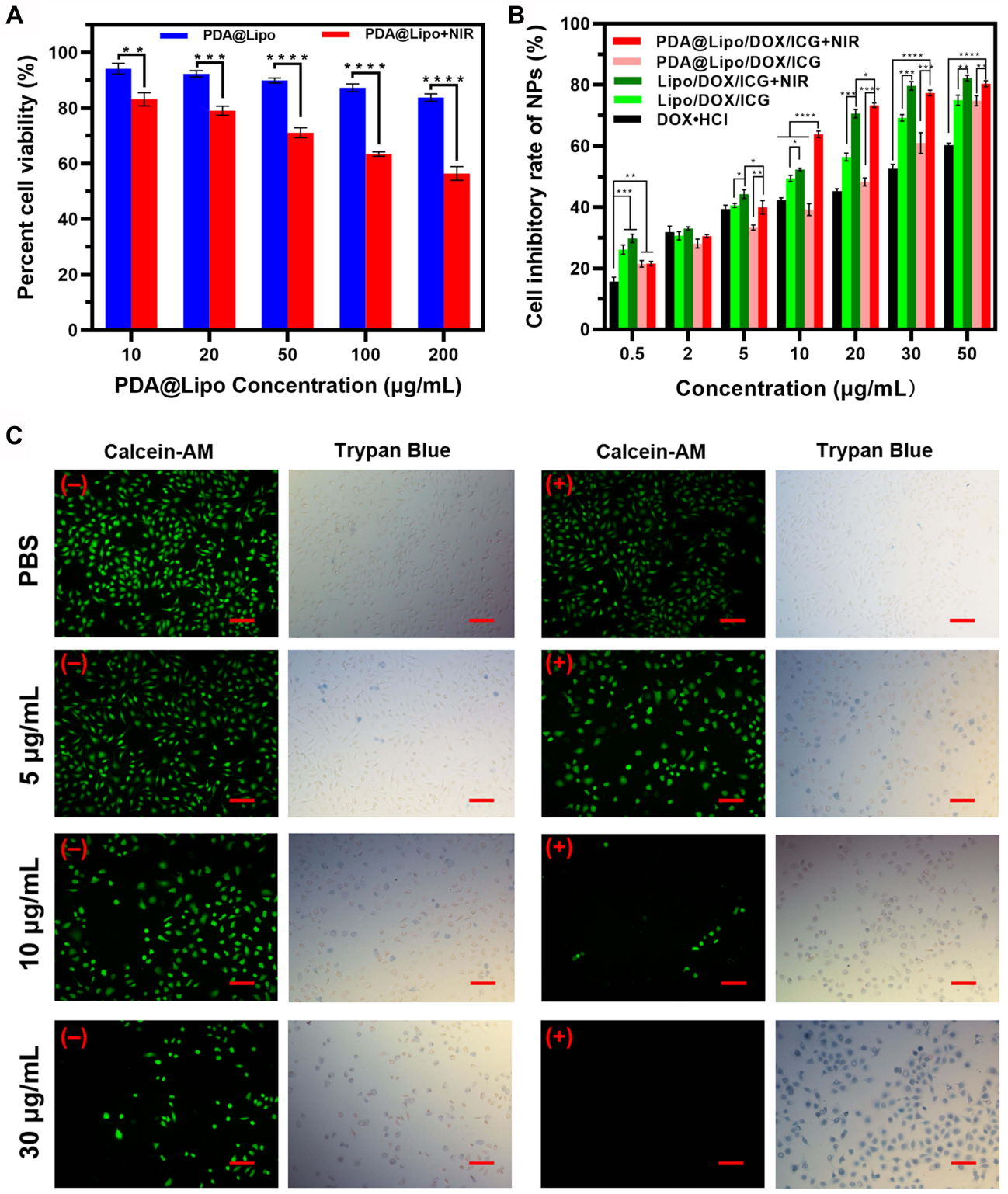

Figure 6 (**A**) MTT assays of blank carrier PDA@Lipo over 24 h in MDA-MB-231 cells with/without irradiation (1.0 W/cm^2, 2 min). (**B**) MTT assays of DOX·HCl, Lipo/DOX@ICG, and PDA@Lipo/DOX@ICG over 24 h in MDA-MB-231 cells with/without irradiation (1.0 W/cm^2, 2 min). (**C**) Fluorescence images of Calcein-AM costained MDA-MB-231 cells (live cells) and bright field images of trypan blue costained MDA-MB-231 cells (dead cells) treated with different concentrations of PDA@Lipo/DOX@ICG (+/– indicated with or without irradiation. The scale bar is 100 μm). (The data are shown as mean ± SD, n = 3 per group, NS, no significance, *p < 0.05, **p < 0.01, ***p < 0.001, ****p < 0.0001).

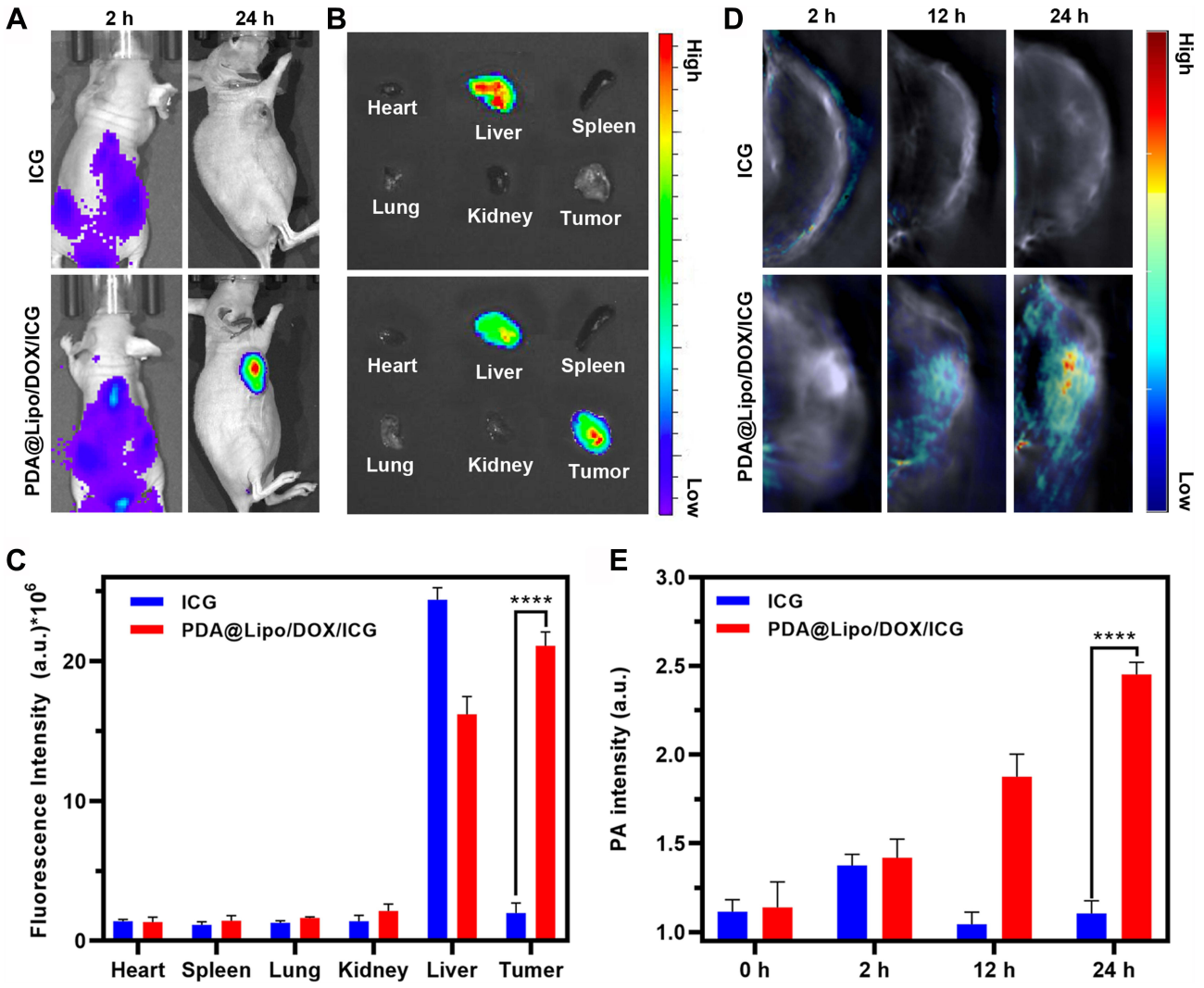

Figure 7 (**A**) Fluorescence images of mice bearing MDA-MB-231 tumors after intravenous injection of free ICG and PDA@Lipo/DOX@ICG at 2 and 24 h. (**B**) Ex vivo FL images of major organs and tumors dissected from mice 24 h post injection of different treatment groups. (**C**) Semiquantitative biodistribution of free ICG and PDA@Lipo/DOX@ICG in mice determined by the averaged Fluorescence intensities of organs and tumor. (**D**) PA images of tumor sites on MDA-MB-231-tumor-bearing mice post injection of free ICG and PDA@Lipo/DOX@ICG at 2, 12, and 24 h. (**E**) The corresponding PA signals at the tumor sites of MDA-MB-231-tumor-bearing mice post injection of free ICG and PDA@Lipo/DOX@ICG at different time points. ****$p < 0.0001$.

The in vivo Antitumor Activity of PDA@Lipo/DOX/ICG

Owing to the excellent imaging ability, photothermal performance of PDA@Lipo/DOX/ICG and the imaging-guided antitumor therapy were subsequently investigated in vivo. Mice bearing MDA-MB-231 tumors were intravenously injected with PDA@Lipo/DOX/ICG or other control formulations, and their tumors were irradiated with 808 nm laser (1.0 W/cm^2) at 24 h post injection. In vivo thermal images were recorded using an infrared thermal imaging camera at different time periods (Figure 8A). The thermal images show that the temperature of tumor regions in PDA@Lipo/DOX/ICG + NIR group rapidly reaches about 48.4 °C. Compared to PBS + NIR group and Lipo/DOX/ICG + NIR group, PDA@Lipo/DOX/ICG + NIR group shows prominent ability to increase temperature within a short time, demonstrating that PDA@Lipo/DOX/ICG not only could accumulate in tumor sites by passive targeting but also is capable of excellent photothermal conversion ability to kill tumor cells in vivo.

In order to prove the in vivo synergistic phototherapy and chemotherapy of PDA@Lipo/DOX/ICG, the antitumor effect was evaluated by the tumor volumes and body weight changes of tumor-bearing mice, and the visualized photographs of tumor bearing mice were shown in Supplementary Figure S5. During the treatment, compared with PBS and PBS + NIR groups, tumor growth inhibition was displayed in all drug-treated groups (Figure 8B). However, the

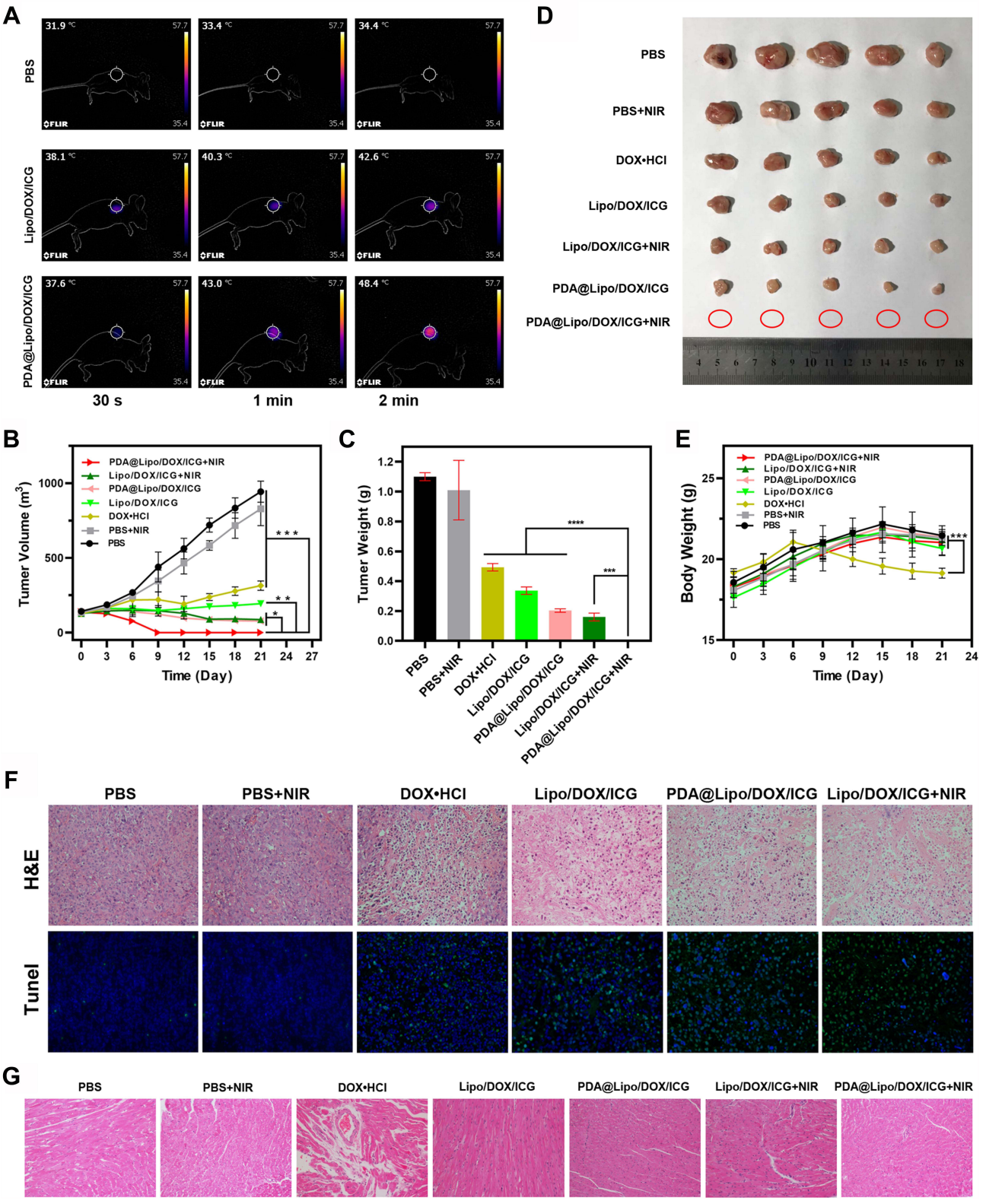

Figure 8 (**A**) Thermal images of MDA-MB-231-tumor-bearing mice from different treating groups (PBS + NIR, Lipo/DOX/ICG + NIR, and PDA@Lipo/DOX@ICG + NIR) under 808 nm laser irradiation for different irradiation periods. (**B**) Tumor volume curves of different groups after various treatments including: PBS, PBS + NIR, DOX·HCl, Lipo/DOX/ICG, PDA@Lipo/DOX@ICG, Lipo/DOX/ICG + NIR, and PDA@Lipo/DOX@ICG + NIR. (**C**) Tumor weights of each group at the end of experiment and IRT. (**D**) Photographs of tumor tissues removed from groups treated with different formulations after 21 d. The red circles indicated disappeared tumors. (**E**) Body weight curves of MDA-MB-231 tumor-bearing mice for each group. (**F**) Representative H&E and Tunel stain images of tumor samples from the treated mice. (**G**) Representative H&E stain images of heart samples from the treated mice. (The data are shown as mean ± SD, n = 5 per group, NS, no significance, *p < 0.05, **p < 0.01, ***p < 0.001, ****p < 0.0001).

tumors could only be partly inhibited by free DOX·HCl, Lipo/DOX/ICG, PDA@Lipo/DOX/ICG, and Lipo/DOX/ICG + NIR groups because of their different deficiencies. In addition, PDA@Lipo/DOX/ICG and Lipo/DOX/ICG + NIR had similar inhibitory effects on tumor volume growth, and both enhanced the antitumor activity than that of free DOX·HCl (Figure 8C). What's more, the tumor growth of PDA@Lipo/DOX/ICG + NIR was completely inhibited and thus no tumors were removed (Figure 8D). The tumors did not recur during the treatment, and the burnt wounds on the skin surface gradually returned to normal, which indicated the best tumor suppression effect. Meanwhile, mice body weight change curves were used to explore the therapeutic efficacy and toxicity. Compared with other six groups, the body weight in free DOX·HCl group was significantly reduced (Figure 8E).

Beyond that, the in vivo toxicity and antitumor efficacy were further evaluated with histological study, in which the tumors and major organs were stained with H&E and Tunel. The results of H&E staining (Figure 8F) show that there were regularly and tightly packed spherical tumor cells in the PBS and PBS + NIR groups, while drug-treated groups exhibited significantly decreased cellularity, tissue fibrosis, and nucleus shrinkage, fragmentation and dissolution, which are typical apoptotic and necrotic characteristics. According to the Tunel staining results, the apoptotic cells of drug-treated groups significantly increased, which are consistent with the results of the in vitro and in vivo antitumor activity experiments (Figures 6 and 8C). In addition, Figure 8G shows the H&E staining images of hearts and there are apparent necrosis of myocardial cells only in free DOX·HCl group because of its cardiotoxicity. Meanwhile, no obvious damage of major organs is observed in each group (Supplementary Figure S6). The histological studies, together with curves of weight change in mice, demonstrate negligible cardiotoxicity and no treatment-induced side effects of PDA@Lipo/DOX/ICG.

Conclusions

In this study, a multifunctional nanoplatform (PDA@Lipo/DOX/ICG) based on PDA-coated liposomes was successfully fabricated, which was loaded with doxorubicin and indocyanine green for combinatorial therapy of breast cancer. At first, polydopamine coating could improve the stability and drug loading of liposomes, and avoid premature drug leakage and unwanted fusion of liposomes. Moreover, surface polydopamine modification can markedly enhance the photothermal conversion efficiency of indocyanine green, and the generated heat could promote the permeation of nanoparticles into tumor cells and the release of doxorubicin. Owing to the synergistic effect of phototherapy and chemotherapy, PDA@Lipo/DOX/ICG displayed a remarkably improved cytotoxicity in MDA-MB-231 cells at relatively low doses. Finally, both indocyanine green and polydopamine can be used as contrast agents for fluorescence imaging (only indocyanine green) and/or photoacoustic imaging and the accumulation of PDA@Lipo/DOX/ICG with obvious signals throughout the treatment could be monitored by the fluorescence imaging and photoacoustic imaging dual-modal imaging.[77] According to our experimental results, PDA@Lipo/DOX/ICG efficiently suppressed the proliferation of MDA-MB-231 cells and even thoroughly ablated tumors, which was far superior to the theranostic outcomes of Lipo/DOX/ICG or doxorubicin hydrochloride groups. Meanwhile, PDA@Lipo/DOX/ICG avoided the cardiotoxicity of doxorubicin hydrochloride groups and no other adverse effects were observed. In summary, this novel nano-system would be a very promising nanoplatform for multi-drug delivery, imaging-guided and multimodal treatments for superior antitumor efficacy.

Abbreviations

DA·HCl, Dopamine hydrochloride; DCFH-DA, 2′, 7′-dichlorofluorescin diacetate; DDSs, Drug delivery systems; DOX, Doxorubicin; DOX·HCl, Doxorubicin hydrochloride; DPBF, 1,3-diphenylisobenzofuran; DSPE-mPEG2000, 1,2-distearoyl-sn-glycero-3-phosphoethanolamine-N-[methoxy(polyethylene glycol)-2000]; EE, Encapsulation efficiency; FBS, Fetal bovine serum; FI, Fluorescence imaging; FTIR, Fourier transform infrared; H&E, Hematoxylin and eosin; HPLC, High-performance liquid chromatography; HSPC, Hydrogenated soybean phosphatidylcholine; ICG, Indocyanine green; IRT, Inhibition rates of tumor growth; LC, Loading capacity; Lipo, Liposomes; MTT, 3-(4,5-Dimethylthiazol-2-yl)-2,5-diphenyltetrazolium bromide; NIR, Near infrared; NPs, Nanoparticles; PAI, Photoacoustic imaging; PDA, Polydopamine; PDIs, Polydispersity indexes; PDT, Photodynamic therapy; PSs, Photosensitizers; PTT, Photothermal therapy; ROS, Reactive oxygen species; SD, Standard deviation.

Data Sharing Statement

All data generated or analyzed during this study are included in this published article and its Supplementary Information Files.

Ethics Approval and Informed Consent

All animal experiments were approved by the Animal Ethics Committee of Central South University and were conducted in compliance with the National Institutes of Health guide for the care and use of Laboratory animals (NIH Publications No. 8023, revised 1978), as well as the internationally recognized `3Rs" principles of animal experiments.

Consent for Publication

All authors agreed to publish this manuscript.

Author Contributions

All authors made significant contributions to the manuscript in all areas of conceptualization, study design, data, and analysis. All authors have participated in drafting or writing, or have substantially revised or critically reviewed the manuscript. All authors have read and approved the final manuscript prior to submission. All authors have agreed on the journal to which the manuscript will be submitted. All authors agree to take responsibility and are accountable for the content of the manuscript.

Funding

This research was supported by National Natural Science Foundation of China (Grant No. 82073932).

Disclosure

The authors declare that they have no competing interests.

References

1. Bray F, Ferlay J, Soerjomataram I, Siegel RL, Torre LA, Jemal A. Global cancer statistics 2018: GLOBOCAN estimates of incidence and mortality worldwide for 36 cancers in 185 countries (vol 68, pg 394, 2018). *CA Cancer J Clin*. 2020;704:313. doi:10.3322/caac.21609
2. Yi HX, Lu WX, Liu F, et al. ROS-responsive liposomes with NIR light-triggered doxorubicin release for combinatorial therapy of breast cancer. *J Nanobiotechnol*. 2021;191:134. doi:10.1186/s12951-021-00877-6
3. Zhang YC, Zeng PY, Ma ZQ, et al. A pH-responsive complex based on supramolecular organic framework for drug-resistant breast cancer therapy. *Drug Deliv*. 2022;291:128–137. doi:10.1080/10717544.2021.2021325
4. Li HZ, Xu W, Li F, et al. Amplification of anticancer efficacy by co-delivery of doxorubicin and lonidamine with extracellular vesicles. *Drug Deliv*. 2022;291:192–202. doi:10.1080/10717544.2021.2023697
5. Sun LH, Li Q, Zhang L, Xu ZG, Kang YJ, Xue P. PEGylated polydopamine nanoparticles incorporated with indocyanine green and doxorubicin for magnetically guided multimodal cancer therapy triggered by near-infrared light. *Acs Appl Nano Mater*. 2018;11:325–336. doi:10.1021/acsanm.7b00176
6. Li PF, Lin BQ, Chen ZA, et al. Biodegradable hollow mesoporous organosilica nanotheranostics (HMONs) as a versatile platform for multimodal imaging and phototherapeutic-triggered endolysosomal disruption in ovarian cancer. *Drug Deliv*. 2022;291:161–173. doi:10.1080/10717544.2021.2021322
7. Dong YX, Zhou L, Shen ZJ, et al. Iodinated cyanine dye-based nanosystem for synergistic phototherapy and hypoxia-activated bioreductive therapy. *Drug Deliv*. 2022;291:238–253. doi:10.1080/10717544.2021.2023701
8. Zhang XG, Cheng LL, Lu Y, et al. A MXene-based bionic cascaded-enzyme nanoreactor for tumor phototherapy/enzyme dynamic therapy and hypoxia-activated chemotherapy. *Nanomicro Lett*. 2022;141:22. doi:10.1007/s40820-021-00761-w
9. Tang R, Dang M, Zhang XJ, et al. Disrupting stromal barriers to enhance photothermal-chemo therapy using a halofuginone-loaded Janus mesoporous nanoplatform. *J Colloid Interface Sci*. 2022;610:313–320. doi:10.1016/j.jcis.2021.11.190
10. Sun XH, Wang J, Wang ZY, et al. Gold nanorod@void@polypyrrole yolk@shell nanostructures: synchronous regulation of photothermal and drug delivery performance for synergistic cancer therapy. *J Colloid Interface Sci*. 2022;610:89–97. doi:10.1016/j.jcis.2021.11.189
11. Mo ZM, Qiu MJ, Zhao K, et al. Multifunctional phototheranostic nanoplatform based on polydopamine-manganese dioxide-IR780 iodide for effective magnetic resonance imaging-guided synergistic photodynamic/photothermal therapy. *J Colloid Interface Sci*. 2022;611:193–204. doi:10.1016/j.jcis.2021.12.071
12. Torres AE, Lyons AB, Hamzavi IH, Lim HW. Response to: "commentary on 'role of phototherapy in the era of biologics'". *J Am Acad Dermatol*. 2021;842. doi:10.1016/j.jaad.2020.09.040
13. Wang MF, Hou ZY, Al Kheraif AA, Xing BG, Lin J. Mini review of TiO2-based multifunctional nanocomposites for near-infrared light-responsive phototherapy. *Adv Healthc Mater*. 2018;720:1800351. doi:10.1002/adhm.201800351
14. Yang S, Chen C, Qiu Y, Xu C, Yao J. Paying attention to tumor blood vessels: cancer phototherapy assisted with nano delivery strategies. *Biomaterials*. 2021;268:120562. doi:10.1016/j.biomaterials.2020.120562

15. Liu Y, Zhen WY, Jin LH, et al. All-in-one theranostic nanoagent with enhanced reactive oxygen species generation and modulating tumor microenvironment ability for effective tumor eradication. *Acs Nano*. 2018;125:4886–4893. doi:10.1021/acsnano.8b01893
16. Liu CH, Wang DD, Zhang SY, et al. Biodegradable biomimic copper/manganese silicate nanospheres for chemodynamic/photodynamic synergistic therapy with simultaneous glutathione depletion and hypoxia relief. *Acs Nano*. 2019;134:4267–4277. doi:10.1021/acsnano.8b09387
17. Yao C, Wang WX, Wang PY, Zhao MY, Li XM, Zhang F. Near-infrared upconversion mesoporous cerium oxide hollow biophotocatalyst for concurrent pH-/H2O2-responsive O-2-evolving synergetic cancer therapy. *Adv Mater*. 2018;307:1704833. doi:10.1002/adma.201704833
18. Huang CL, Zhang ZM, Guo Q, et al. A dual-model imaging theragnostic system based on mesoporous silica nanoparticles for enhanced cancer phototherapy. *Adv Healthc Mater*. 2019;819:1900840. doi:10.1002/adhm.201900840
19. Pei Q, Hu XL, Zheng XH, et al. Light-activatable red blood cell membrane-camouflaged dimeric prodrug nanoparticles for synergistic photodynamic/chemotherapy. *Acs Nano*. 2018;122:1630–1641. doi:10.1021/acsnano.7b08219
20. Yang GB, Xu LG, Xu J, et al. Smart nanoreactors for pH-responsive tumor homing, mitochondria-targeting, and enhanced photodynamic-immunotherapy of cancer. *Nano Lett*. 2018;184:2475–2484. doi:10.1021/acs.nanolett.8b00040
21. Liang S, Deng XR, Chang Y, et al. Intelligent hollow Pt-CuS janus architecture for synergistic catalysis-enhanced sonodynamic and photothermal cancer therapy. *Nano Lett*. 2019;196:4134–4145. doi:10.1021/acs.nanolett.9b01595
22. Li W, Yang J, Luo LH, et al. Targeting photodynamic and photothermal therapy to the endoplasmic reticulum enhances immunogenic cancer cell death. *Nat Commun*. 2019;10:3349. doi:10.1038/s41467-019-11269-8
23. Gao Y, Zhang LY, Liu YH, et al. Ce6/Mn2+-chelated polydopamine@black-TiO2 nanoprobes for enhanced synergistic phototherapy and magnetic resonance imaging in 4T1 breast cancer. *Nanoscale*. 2020;123:1801–1810. doi:10.1039/c9nr09236f
24. Terentyuk G, Panfilova E, Khanadeev V, et al. Gold nanorods with a hematoporphyrin-loaded silica shell for dual-modality photodynamic and photothermal treatment of tumors in vivo. *Nano Res*. 2014;73:325–337. doi:10.1007/s12274-013-0398-3
25. Fan WP, Yung B, Huang P, Chen XY. Nanotechnology for multimodal synergistic cancer therapy. *Chem Rev*. 2017;11722:13566–13638. doi:10.1021/acs.chemrev.7b00258
26. Hu JJ, Luo HH, Qu Q, et al. Cell membrane-inspired polymeric vesicles for combined photothermal and photodynamic prostate cancer therapy. *ACS Appl Mater Interfaces*. 2020;1238:42511–42520. doi:10.1021/acsami.0c11636
27. Miao WJ, Kim HJ, Gujrati V, et al. Photo-decomposable organic nanoparticles for combined tumor optical imaging and multiple phototherapies. *Theranostics*. 2016;613:2367–2379. doi:10.7150/thno.15829
28. Liao JF, Li WT, Peng JR, et al. Combined cancer photothermal-chemotherapy based on doxorubicin/gold nanorod-loaded polymersomes. *Theranostics*. 2015;54:345–356. doi:10.7150/thno.10731
29. Zhu XJ, Li JC, Qiu XC, Liu Y, Feng W, Li FY. Upconversion nanocomposite for programming combination cancer therapy by precise control of microscopic temperature. *Nat Commun*. 2018;9:2176. doi:10.1038/s41467-018-04571-4
30. Chen HZ, Zeng XW, Tham HP, et al. NIR-light-activated combination therapy with a precise ratio of photosensitizer and prodrug using a host-guest strategy. *Angew Chem Int Edit*. 2019;5823:7641–7646. doi:10.1002/anie.201900886
31. Guan SY, Weng YZW, Li MN, et al. An NIR-sensitive layered supramolecular nanovehicle for combined dual-modal imaging and synergistic therapy. *Nanoscale*. 2017;929:10367–10374. doi:10.1039/c7nr01771e
32. Guo Y, Jiang K, Shen ZC, et al. A small molecule nanodrug by self-assembly of dual anticancer drugs and photosensitizer for synergistic near-infrared cancer theranostics. *ACS Appl Mater Interfaces*. 2017;950:43508–43519. doi:10.1021/acsami.7b14755
33. Gao S, Wang GH, Qin ZN, et al. Oxygen-generating hybrid nanoparticles to enhance fluorescent/photoacoustic/ultrasound imaging guided tumor photodynamic therapy. *Biomaterials*. 2017;112:324–335. doi:10.1016/j.biomaterials.2016.10.030
34. Guo W, Guo CS, Zheng NN, Sun TD, Liu SQ. CsxWO3 nanorods coated with polyelectrolyte multilayers as a multifunctional nanomaterial for bimodal imaging-guided photothermal/ photodynamic cancer treatment. *Adv Mater*. 2017;294:1604157. doi:10.1002/adma.201604157
35. Lv YQ, Xu CR, Zhao XM, et al. Nanoplatform assembled from a CD44-targeted prodrug and smart liposomes for dual targeting of tumor microenvironment and cancer cells. *Acs Nano*. 2018;122:1519–1536. doi:10.1021/acsnano.7b08051
36. Yan F, Duan WL, Li YK, et al. NIR-laser-controlled drug release from DOX/IR-780-loaded temperature-sensitive-liposomes for chemo-photothermal synergistic tumor therapy. *Theranostics*. 2016;613:2337–2351. doi:10.7150/thno.14937
37. Brito J, Hlushko H, Abbott A, Aliakseyeu A, Hlushko R, Sukhishvili SA. Integrating antioxidant functionality into polymer materials: fundamentals, strategies, and applications. *ACS Appl Mater Interfaces*. 2021;1335:41372–41395. doi:10.1021/acsami.1c08061
38. Lee YH, Chang DS. Fabrication, characterization, and biological evaluation of anti-HER2 indocyanine green-doxorubicin-encapsulated PEG-b-PLGA copolymeric nanoparticles for targeted photochemotherapy of breast cancer cells. *Sci Rep*. 2017;7:46688. doi:10.1038/srep46688
39. Wang HL, Li XX, Tse BW-C, et al. Indocyanine green-incorporating nanoparticles for cancer theranostics. *Theranostics*. 2018;8(5):1227–1242. doi:10.7150/thno.22872
40. Paris JL, Baeza A, Vallet-Regi M. Overcoming the stability, toxicity, and biodegradation challenges of tumor stimuli-responsive inorganic nanoparticles for delivery of cancer therapeutics. *Expert Opin Drug Deliv*. 2019;1610:1095–1112. doi:10.1080/17425247.2019.1662786
41. Al-Jamal WT, Kostarelos K. Liposomes: from a clinically established drug delivery system to a nanoparticle platform for theranostic nanomedicine. *Acc Chem Res*. 2011;4410:1094–1104. doi:10.1021/ar200105p
42. Stavnsbjerg C, Christensen E, Munter R, et al. Accelerated blood clearance and hypersensitivity by PEGylated liposomes containing TLR agonists. *J Control Release*. 2022;342:337–344. doi:10.1016/j.jconrel.2021.12.033
43. Amin M, Mansourian M, Koning GA, Badiee A, Jaafari MR, ten Hagen TLM. Development of a novel cyclic RGD peptide for multiple targeting approaches of liposomes to tumor region. *J Control Release*. 2015;220:308–315. doi:10.1016/j.jconrel.2015.10.039
44. Russell LM, Hultz M, Searson PC. Leakage kinetics of the liposomal chemotherapeutic agent doxil: the role of dissolution, protonation, and passive transport, and implications for mechanism of action. *J Control Release*. 2018;269:171–176. doi:10.1016/j.jconrel.2017.11.007
45. Hu XL, Zhai SD, Liu GH, Xing D, Liang HJ, Liu SY. Concurrent drug unplugging and permeabilization of polyprodrug-gated crosslinked vesicles for cancer combination chemotherapy. *Adv Mater*. 2018;3021:1706307. doi:10.1002/adma.201706307
46. Bleher S, Buck J, Muhl C, et al. Poly(sarcosine) surface modification imparts stealth-like properties to liposomes. *Small*. 2019;1550:1904716. doi:10.1002/smll.201904716
47. de Oliveira JK, Ueda-Nakamura T, Correa AG, et al. Liposome-based nanocarrier loaded with a new quinoxaline derivative for the treatment of cutaneous leishmaniasis. *Mater Sci Eng C*. 2020;110:110720. doi:10.1016/j.msec.2020.110720

48. Zhang N, Cai XJ, Gao W, et al. A multifunctional theranostic nanoagent for dual-mode image-guided HIFU/chemo-synergistic cancer therapy. *Theranostics*. 2016;63:404–417. doi:10.7150/thno.13478
49. Lu JH, Cai LL, Dai Y, et al. Polydopamine-based nanoparticles for photothermal therapy/chemotherapy and their synergistic therapy with autophagy inhibitor to promote antitumor treatment. *Chem Rec*. 2021;214:781–796. doi:10.1002/tcr.202000170
50. Singh I, Priyam A, Jha D, Dhawan G, Gautam HK, Kumar P. Polydopamine -aminoglycoside nanoconjugates: synthesis, characterization, antimicrobial evaluation and cytocompatibility. *Mater Sci Eng C*. 2020;107:110284. doi:10.1016/j.msec.2019.110284
51. Xu X, Li YL, Wang LX, et al. Triple-functional polyetheretherketone surface with enhanced bacteriostasis and anti-inflammatory and osseointegrative properties for implant application. *Biomaterials*. 2019;212:98–114. doi:10.1016/j.biomaterials.2019.05.014
52. Bi DD, Zhao L, Li HW, Guo YF, Wang XT, Han MH. A comparative study of polydopamine modified and conventional chemical synthesis method in doxorubicin liposomes form the aspect of tumor targeted therapy. *Int J Pharm*. 2019;559:76–85. doi:10.1016/j.ijpharm.2019.01.033
53. Xie XZ, Mao CY, Liu XM, et al. Tuning the bandgap of photo-sensitive polydopamine/Ag3PO4/graphene oxide coating for rapid, noninvasive disinfection of implants. *ACS Cent Sci*. 2018;46:724–738. doi:10.1021/acscentsci.8b00177
54. Shim NY, Heo JS. Performance of the polydopamine-graphene oxide composite substrate in the osteogenic differentiation of mouse embryonic stem cells. *Int J Mol Sci*. 2021;2214:7323. doi:10.3390/ijms22147323
55. Wang Y, Zhang Y, Jin M, Lv YH, Pei ZC, Pei YX. A hypericin delivery system based on polydopamine coated cerium oxide nanorods for targeted photodynamic therapy. *Polymers-Basel*. 2019;116:1025. doi:10.3390/polym11061025
56. Awasthi AK, Gupta S, Thakur J, et al. Polydopamine-on-liposomes: stable nanoformulations, uniform coatings and superior antifouling performance. *Nanoscale*. 2020;128:5021–5030. doi:10.1039/c9nr07770g
57. Wu Q, Niu M, Chen XW, et al. Biocompatible and biodegradable zeolitic imidazolate framework/polydopamine nanocarriers for dual stimulus triggered tumor thermo-chemotherapy. *Biomaterials*. 2018;162:132–143. doi:10.1016/j.biomaterials.2018.02.022
58. Zheng XY, Chen F, Zhang JX, Cai KY. Silica-assisted incorporation of polydopamine into the framework of porous nanocarriers by a facile one-pot synthesis. *J Mater Chem B*. 2016;414:2435–2443. doi:10.1039/c5tb02784e
59. Wang Z, Duan Y, Duan YW. Application of polydopamine in tumor targeted drug delivery system and its drug release behavior. *J Control Release*. 2018;290:56–74. doi:10.1016/j.jconrel.2018.10.009
60. Wang JL, Wang R, Zhang FR, et al. Overcoming multidrug resistance by a combination of chemotherapy and photothermal therapy mediated by carbon nanohorns. *J Mater Chem B*. 2016;436:6043–6051. doi:10.1039/c6tb01469k
61. Entradas T, Waldron S, Volk M. The detection sensitivity of commonly used singlet oxygen probes in aqueous environments. *J Photochem Photobiol B*. 2020;204:111787. doi:10.1016/j.jphotobiol.2020.111787
62. Kiesslich T, Gollmer A, Maisch T, Berneburg M, Plaetzer K. A comprehensive tutorial on in vitro characterization of new photosensitizers for photodynamic antitumor therapy and photodynamic inactivation of microorganisms. *Biomed Res Int*. 2013;2013:840417. doi:10.1155/2013/840417
63. Liu SP, Zheng ZQ, Wang S, et al. Polydopamine-coated chitosan/calcium pyrophosphate hybrid microflowers as an effective hemostatic agent. *Carbohydr Polym*. 2019;224:115175. doi:10.1016/j.carbpol.2019.115175
64. Cheng W, Liang CY, Xu L, et al. TPGS-functionalized polydopamine-modified mesoporous silica as drug nanocarriers for enhanced lung cancer chemotherapy against multidrug resistance. *Small*. 2017;1329:1700623. doi:10.1002/smll.201700623
65. Tanaka T, Shiramoto S, Miyashita M, Fujishima Y, Kaneo Y. Tumor targeting based on the effect of enhanced permeability and retention (EPR) and the mechanism of receptor-mediated endocytosis (RME). *Int J Pharm*. 2004;277(1–2):39–61. doi:10.1016/j.ijpharm.2003.09.050
66. Huang RL, Liu X, Ye HJ, et al. Conjugation of hyaluronic acid onto surfaces via the interfacial polymerization of dopamine to prevent protein adsorption. *Langmuir*. 2015;3144:12061–12070. doi:10.1021/acs.langmuir.5b02320
67. Zhao JW, Li X, Wang X, Wang X. Fabrication of hybrid nanostructures based on Fe3O4 nanoclusters as theranostic agents for magnetic resonance imaging and drug delivery. *Nanoscale Res Lett*. 2019;14:200. doi:10.1186/s11671-019-3026-7
68. Jose I, Vishnoi G, Deodhar K, Desai U. Non-invasive imaging of breast cancer: synthesis and study of novel near-infrared fluorescent estrogen conjugate. *Lect Notes Comput Sci*. 2005;5693:521–527. doi:10.1117/12.589571
69. Farrakhova D, Romanishkin I, Maklygina Y, Bezdetnaya L, Loschenov V. Analysis of fluorescence decay kinetics of indocyanine green monomers and aggregates in brain tumor model in vivo. *Nanomater Basel*. 2021;1112:3185. doi:10.3390/nano11123185
70. Farrakhova D, Maklygina Y, Romanishkin I, et al. Fluorescence imaging analysis of distribution of indocyanine green in molecular and nanoform in tumor model. *Photodiagnosis Photodyn*. 2022;37:102636. doi:10.1016/j.pdpdt.2021.102636
71. Sobotta L, Fita P, Szczolko W, et al. Functional singlet oxygen generators based on porphyrazines with peripheral 2,5-dimethylpyrrol-1-yl and dimethylamino groups. *J Photoch Photobio A*. 2013;269:9–16. doi:10.1016/j.jphotochem.2013.06.018
72. Zhan YH, Zhan WH, Li HR, et al. In vivo dual-modality fluorescence and magnetic resonance imaging-guided lymph node mapping with good biocompatibility manganese oxide nanoparticles. *Molecules*. 2017;2212:2208. doi:10.3390/molecules22122208
73. Chen SY, Miao H, Jiang XY, Sun PF, Fan QL, Huang W. Starlike polymer brush-based ultrasmall nanoparticles with simultaneously improved NIR-II fluorescence and blood circulation for efficient orthotopic glioblastoma imaging. *Biomaterials*. 2021;275:120916. doi:10.1016/j.biomaterials.2021.120916
74. Tian YA, Zhao D, Huang XY, Guan XM, Wang F, Wei XB. Extended it-conjugative carbon nitride for single 1064 nm laser-activated photodynamic/photothermal synergistic therapy and photoacoustic imaging. *ACS Appl. Mater Interfaces*. 2022. doi:10.1021/acsami.1c22481
75. Zhang MH, Kim HS, Jin TF, Yi A, Moon WK. Ultrasound-guided photoacoustic imaging for the selective detection of EGFR-expressing breast cancer and lymph node metastases. *Biomed Opt Express*. 2016;75:1920–1931. doi:10.1364/Boe.7.001920
76. Zafar H, Breathnach A, Subhash HM, Leahy MJ. Photoacoustic imaging of the human forearm using 40 MHz linear-array transducer. *Proc Spie*. 2014;8942. doi:10.1117/12.2040637
77. Lin LS, Cong ZX, Cao JB, et al. Multifunctional Fe3O4@polydopamine core-shell nanocomposites for intracellular mRNA detection and imaging-guided photothermal therapy. *Acs Nano*. 2014;84:3876–3883. doi:10.1021/nn500722y